11-2013

Core-leaf onion-like carbon/MnO2 hybrid nano-urchins for rechargeable lithium-ion batteries

Ye Wang
Singapore University of Technology and Design

Zhao Jun Han
CSIRO

Siu Fung Yu
Hong Kong Polytechnic University

Ran Ran Song
Beijing University of Chemical Technology

Huai He Song
Beijing University of Chemical Technology

See next page for additional authors

Core-leaf onion-like carbon/MnO2 hybrid nano-urchins for rechargeable lithium-ion batteries

Abstract

A hybrid nano-urchin structure consisting of spherical onion-like carbon and MnO2 nanosheets is synthesized by a facile and environmentally-friendly hydrothermal method. Lithium-ion batteries incorporating the hybrid nano-urchin anode exhibit reversible lithium storage with superior specific capacity, enhanced rate capability, stable cycling performance, and nearly 100% Coulombic efficiency. These results demonstrate the effectiveness of designing hybrid nano-architectures with uniform and isotropic structure, high loading of electrochemically-active materials, and good conductivity for the dramatic improvement of lithium storage.

Disciplines

Engineering | Physical Sciences and Mathematics

Publication Details

Wang, Y., Han, Z., Yu, S., Song, R., Song, H., Ostrikov, K. & Yang, H. (2013). Core-leaf onion-like carbon/MnO2 hybrid nano-urchins for rechargeable lithium-ion batteries. Carbon, 64 (November), 230-236.

Authors

Ye Wang, Zhao Jun Han, Siu Fung Yu, Ran Ran Song, Huai He Song, Kostya (Ken) Ostrikov, and Hui Ying Yang

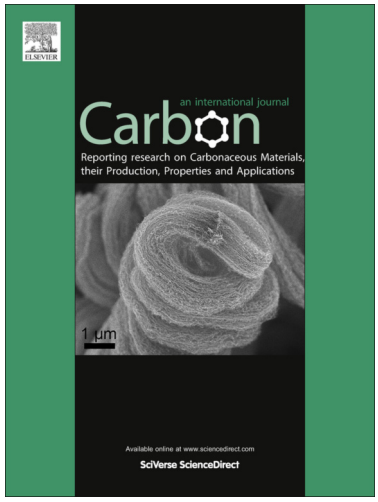

Core-leaf onion-like carbon/MnO_2 hybrid nano-urchins for rechargeable lithium-ion batteries

Ye Wang, Zhao Jun Han, Siu Fung Yu, Ran Ran Song, Huai He Song, Kostya Ken Ostrikov, Hui Ying Yang

PII: S0008-6223(13)00691-X
DOI: http://dx.doi.org/10.1016/j.carbon.2013.07.057
Reference: CARBON 8238

To appear in: *Carbon*

Received Date: 4 April 2013
Accepted Date: 20 July 2013

Please cite this article as: Wang, Y., Han, Z.J., Yu, S.F., Song, R.R., Song, H.H., Ostrikov, K.K., Yang, H.Y., Core-leaf onion-like carbon/MnO_2 hybrid nano-urchins for rechargeable lithium-ion batteries, *Carbon* (2013), doi: http://dx.doi.org/10.1016/j.carbon.2013.07.057

Core-leaf onion-like carbon/MnO_2 hybrid nano-urchins for rechargeable lithium-ion batteries

Ye Wang [a], Zhao Jun Han [b], Siu Fung Yu [c], Ran Ran Song [d], Huai He Song [d], Kostya (Ken) Ostrikov [b,e,f], Hui Ying Yang [a,1]

[a] *Pillar of Engineering Product Development, Singapore University of Technology and Design, 20 Dover Drive, 138682, Singapore*

[b] *CSIRO Materials Science and Engineering, P.O. Box 218, Lindfield, New South Wales 2070, Australia*

[c] *Department of Applied Physics, The Hong Kong Polytechnic University, Hung Hom, Kowloon, Hong Kong*

[d] *State Key Laboratory of Chemical Resource Engineering, Key Laboratory of Carbon Fibre and Functional Polymers, Ministry of Eduction, Beijing University of Chemical Technology, Beijing 100029, P. R. China*

[e] *School of Physics, The University of Sydney, New South Wales 2006, Australia*

[f] *Australian Institute for Innovative Materials, The University of Wollongong, New South Wales 2522, Australia*

[1] Corresponding author. Tel.: +65 6303 6663. E-mail address: yanghuiying@sutd.edu.sg (H. Y. Yang)

ABSTRACT

A hybrid nano-urchin structure consisting of spherical onion-like carbon and MnO_2 nanosheets is synthesized by a facile and environmentally-friendly hydrothermal method. Lithium-ion batteries incorporating the hybrid nano-urchin anode exhibit reversible lithium storage with superior specific capacity, enhanced rate capability, stable cycling performance, and nearly 100% Coulombic efficiency. These results demonstrate the effectiveness of designing hybrid nano-architectures with uniform and isotropic structure, high loading of electrochemically-active materials, and good conductivity for the dramatic improvement of lithium storage.

1. Introduction

Developing high-performance rechargeable lithium-ion batteries (LIBs) is among the most promising solutions to address the drastic increase in global demand of energy [1]. LIBs were introduced to the market in the 1990s by Sony and soon attracted a strong research interest due to their high energy density, stability, and no memory effect, as compared to other alternatives [2]. However, commercial LIBs mostly use graphite as the anode material, which possesses a relatively low theoretical specific capacity of ~372 mAh g^{-1}. This low capacity severely hampers the wide usage of LIBs in the surging consumer electronic devices and the large-scale energy applications such as hybrid electric vehicles, renewable power plants, and load levelling [3-5]. To accommodate the high-level requirements of these advanced applications, it is imperative to explore new electrode materials and novel designs for higher energy density, lower cost, flexibility, non-toxicity, and better stability.

The recent advances in nanotechnology have offered a promising route to tackle these challenges [6-9]. As compared to the bulk materials, nanostructured materials possess a large surface area with excellent electrical, optical, and mechanical properties. Nanomaterials can enhance the performance of LIBs through two approaches. The first one is by using low-dimensional carbon-based nanomaterials to provide more efficient lithiation and delithiation processes. For instance, *Endo et al.* firstly demonstrated the possibility of incorporating submicron vapour grown carbon fibres (VGCFs) into the anode of LIBs [10]; *Hu et al.* used free-standing carbon nanotube (CNT) film to fabricate flexible LIBs [11]; more recently, graphene and ultrathin graphite foams were utilized to offer higher energy capacity of LIBs [12]. The other approach is by using metal oxide nanoparticles or conductive polymers to store lithium through electrochemical redox reactions. A wide range of nanoparticles such as Si, Ge, Fe_3O_4, Fe_2O_3, Co_3O_4, and Cu_2O have been successfully implemented to improve the

performance of LIBs. Moreover, hybrid nanostructures which combine the advantages from both carbon nanomaterials and metal oxide nanoparticles were also demonstrated [13-16].

Among various metal oxide nanoparticles, manganese oxides (MO_x) which can be synthesized with different structure (*e.g.*, crystalline or amorphous) and multiple-valent state (*e.g.*, MnO, Mn_2O_3, MnO_2, Mn_3O_4) are increasingly recognised as one of the best anode materials for LIBs [17,18]. In particular, MnO_2 nanoparticles are stable, nontoxic and environmentally benign, and have a high specific capacity (~1230 mAh g^{-1}). Much effort is thus devoted to synthesize and control the structure of MnO_2-based materials [19-21]. However, the performance of MnO_2-based anodes remains inferior due to two main issues: (i) the pristine MnO_2 has a low electrical conductivity (10^{-5} – 10^{-6} S/cm) which limits the electron transport; (ii) a large volume change of MnO_2 occurs during the lithiation and delithiation processes, which leads to severe electrode pulverization, serious safety concerns and rapid loss of discharge capacity during the cycling [17,21,22].

Issue (i) can be partially mitigated by coating the MnO_2 nanostructures with highly-conductive carbonaceous materials, such as single- and multi-walled CNTs, graphene, poly(3,4-ethylenedioxythiophene) (PEDOT), and mesoporous carbons [23,24]. However, issue (ii) remains largely unresolved as it is associated with the fundamental charge storage mechanism and the inherent structural properties of MnO_2 nanoparticles. Indeed, the available MnO_2–based LIBs often experience poor cycling performance, low stability, and even cracking, delamination, and crumbling of the anode material [17,25,26].

In this work we solve these problems by fabricating the hybrid nano-urchin structure consisting of onion-like carbon/MnO_2 (OLC/MnO_2) using a simple and environmentally-benign hydrothermal method. The OLC acts as both the support for MnO_2 nanostructures and the conductive core for electron transport. It was chosen because of three prominent features:

the good conductivity which promotes fast electron transport, the large specific surface area which allows a high loading of the electrochemically active MnO_2 nanoparticles, and the isotropic structure which enhances the accessibility of nanoparticles to the electrolyte ions and accommodates the change of volume during lithium storage [27-29]. We demonstrate that LIBs incorporating the hybrid nano-urchin anode exhibit better cycling performance and rate capabilities with nearly 100% Coulombic efficiency, which are significantly improved from that of the pure MnO_2 or OLC anodes. Moreover, the structure of the OLC/MnO_2 hybrid remains distinguishable after more than 100 cycling tests, in a drastic contrast to the pure MnO_2 structure which degraded upon a few cycles of electrochemical operation.

2. EXPERIMENTAL

2.1 Preparation of the core-leaf OLC/MnO_2 hybrid nano-urchins

The synthesis procedure and the proposed nano-assembly mechanism of core-leaf OLC/MnO_2 hybrid nano-urchins are schematically shown in Fig. 1a. Briefly, we firstly prepared MnO_2 nanoparticles on the surface of OLC by stirring the mixture of 150 mg potasium permanganate ($KMnO_4$) and 50 mg OLC in 25 ml de-ionized water at 55 °C for 6 hours in a 50 mL Teflon-line stainless steel autoclave. The intermediate OLC/MnO_2 product was then treated in a simple hydrothermal process at 150 °C for 12 hours to transform into the nano-urchin structure. Pure MnO_2 was also synthesized in a hydrothermal process at 150 ^oC for 3 hours by mixing $KMnO_4$ with H_2SO_4 in DI water.

2.2 Morphological and structural characterizations

Morphology and structure of the samples were examined by the field-emission scanning electron microscopy (FE-SEM, Zeiss LEO 1550) and transmission electron microscopy (TEM, JEOL JEM-2100F). Compositional investigation of the samples was performed by energy-dispersive X-ray spectroscopy (EDX, JEOL JSM-5910LV). The crystal structure of samples was investigated by X-ray diffaction (XRD, Siemens D5005) with Cu Ka (λ=0.154 nm) radiation and the accelerating voltage of 40 kV. Thermal weight changes was measured by thermogravimetric analysis (TGA, Shimadzu DTG-60). Additionally, surface area analyzer (Micromeritics ASAP 242,) was used to measure the specific surface area with N_2 physisorption at 77 K.

2.3 Electrochemical measurement

The electrochemical properties were investigated by a two-electrode half-cell configuration composed of the lithium foil as the counter electrode and the active material as the working electrode. Typically, electrode slurry was prepared by mixing 80 wt% active material, 10 wt% conductive carbon black and 10 wt% polyvinyldifluoride (PVDF) binder in the *N-Methylpyrrolidone* (NMP) solution. The slurry was then painted onto a nickel-foam current collector, followed by drying in a vacuum oven. The mass of the active material is in the range of 3 – 4 mg cm^{-2}. 1M $LiPF_6$ solution in a 1 : 1 (v : v) mixture of ethylene-carbonate/ethyl-methyl-carbonate (EC/EMC) and Celgard 2400 membranes were employed as the electrolyte and the separator, respectively. All components listed above were assembled into a standard CR2032 button battery in a glove box filled with argon gas. The cyclic voltammetry (CV) and electrochemical impedance spectra (EIS) measurements of the half-cells were carried out on a potentiostat/galvanostat (VMP3, Bio-Logic). The scan rate of the CVs was at 0.05 mV s^{-1} and the frequency range for the EIS spectra was varied from 0.01 Hz to 1 MHz. The galvanostatic discharging/charging test was performed in the potential

range of 0.01 – 3.0 V at various current densities from 50 to 2000 mA g^{-1} using the Neware battery tester.

3. RESULTS AND DISCUSSION

3.1 Morphology and structure of the OLC/MnO_2 nano-urchins

The scanning electron microscopy (SEM) images of the pure OLC, the intermediate product, and the final OLC/MnO_2 nano-urchins are shown in Fig. 1b, 1c, and 1d, respectively. One can see that the size of nanoparticles increased significantly during the hydrothermal process. Bundles of MnO_2 nanosheets were observed to radiate from the OLC core (inset of Fig. 1d and Fig. S1), giving rise to the highly-porous core-leaf structure with a large surface area. Moreover, the diffraction peaks in the XRD measurements of OLC/MnO_2 nano-urchins could be indexed as (001), (002), (110), (111) and (020) planes of the birnessite-type MnO_2 (Fig. S2) [29]. This birnessite-type of MnO_2 is characterized by a layered structure consisting of edge-shared MnO_6 octahedra, which allows high mobility of the interlayer cations with fast kinetics and little structural re-arragement [30]. Some MnO_2 nanofibers were also found in the final product (Fig. 1c), which can be attributed to the transformation from birnessite-type MnO_2 nanosheets into nanofibers at extended reaction time and/or high temperature [31,32]. The hybrid OLC/MnO_2 was therefore architectured into an intricate, three-dimensional (3D) urchin-like structure with an isotropic surface, which can effectively reduce the aggregation of Mn metal formed during the electrochemical reaction and enhance the cyclic stability, as demonstrated in detail below.

Figure 2 shows the crystalline structure and compositional analysis of the pure OLC and OLC/MnO_2 nano-urchins obtained by TEM and EDX. Pure OLC had a highly-crystalline graphitic wall structure with an interplanar spacing of 0.34 nm [the (002) basal plane] and a

diameter of about 15 – 40 nm (Fig. 2a and 2b). When coated with MnO_2, the size of the core-leaf structure increased to 200 – 300 nm with the length of MnO_2 nanosheets of ~100 nm (Fig. 2c and 2d). We noted that the density of MnO_2 was much higher in the present case than that grown on hollow carbon spheres (diameter of ~200 nm) [33], making the current nanostructure promising for higher energy storage capacity. The specific surface area of pure OLC was 377 m^2 g^{-1} as calculated by the Brunauer–Emmett–Teller (BET) method (Fig. S3). This large surface area of OLC might thus contribute to the high loading of MnO_2 nanoparticles.

TEM images further indicated that the interplanar spacing of birnessite-type MnO_2 nanosheets was ~0.7 nm (Fig. 2d–2e and Fig. S1), in a good agreement with others [20,34]. The multiple diffraction rings observed in the selected-area electron diffraction (SAED) pattern suggested that MnO_2 was nanocrystalline (Fig. 2f). According to *Xia et al.* [35], when the $KMnO_4$ solution is mixed with carbon nanomaterials before the hydrothermal processing, the nanocrystalline MnO_2 forms on the surface of carbon nanomaterials due to the slow redox process according to the following Eq. (1).

$$4MnO_4^- + 3C + H_2O \rightarrow 4MnO_2 + CO_3^{2-} + 2HCO_3^- \quad (1)$$

When the solution is further treated in the hydrothermal reaction, the MnO_2 nanosheets grow from the preformed nanocrystalline due to the decomposition of $KMnO_4$ in water according to Eq. (2).

$$4MnO_4^- + 2H_2O \rightarrow 4MnO_2 + 4OH^- + 3O_2 \quad (2)$$

In addition, we have previously shown that water molecules and potassium ions may diffuse into the interlayer of birnessite-type MnO_2 during the synthesis process [29]. This presence of potassium ions is beneficial for stabilizing the layered structure of MnO_2 [30]. It is estimated here from the EDX spectrum that the K/Mn ratio was about 0.23 (Fig. 2g and Table S1). Moreover, the TGA results of OLC/MnO_2 nano-urchins indicated that the water

content and OLC was about 9% and 17%, respectively (Fig. S4). The interlayer water is then calculated about 0.64 H_2O per chemical formula, *i.e.*, $K_{0.23}MnO_2 \cdot 0.64H_2O$ [35]. The final product of the nano-urchins was thus denoted as $0.83(K_{0.23}MnO_2 \cdot 0.64H_2O)/0.17OLC$.

3.2 Lithium storage performance

Next, we fabricated a standard CR2032 button half-cell battery with the 3D OLC/MnO_2 nano-urchins as the working electrode and the lithium foil as the counter electrode in a glove box filled with Ar (a photo is shown as the inset of Fig. 3b). It is known that the mechanism of lithium reacting with nano-sized MnO_2 (also other *3d*-metal oxides such as CoO_x and MoO_x) differs from the classical lithium intercalation or alloying processes; instead, it is a reversible redox reaction process involving the formation of Li_2O,

$$MnO_2 + 4Li^+ + 4e^- \leftrightarrow 2Li_2O + Mn \quad (3)$$

followed by the decomposition of Li_2O and oxidation of metallic nanoparticles [19,35].

Figure 3a shows the CV curves of OLC/MnO_2 core-leaf nano-urchins in the first three cycles, obtained at a scan rate of 0.05 mV/s and a potential window of 0.01 – 3 V *vs* Li/Li^+. One can see that in the first cathodic cycle there was one weak peak at 0.75 V and one main peak near 0.24 V. The former corresponded to the possible reduction of Mn^{4+} to Mn^{2+}, while the latter was associated with the complete reduction of Mn^{2+} to Mn and the formation of a solid electrolyte interface (SEI) layer at the interface of electrolyte and electrode (a polymer/gel-like film which allowed only lithium ions to diffuse) [36,37]. From the second cathodic cycle, the weak peak disappeared and the main reduction peak shifted to 0.3 V, indicating the reversible phase transformation as given in Eq. (3).

In the anodic process of Fig. 3a, one main peak was observed at around 1.3 V and one weak peak at 2.1 V, corresponding to the oxidation of metallic Mn to Mn^{2+} and the

decomposition of polymer/gel film related to the SEI layer [37]. These peaks were similar to those of pure MnO_2 but different from those of pure OLC (Fig. S5a and S5b), confirming that the MnO_2 nanosheets were the main medium for lithium storage.

The galvanostatic discharging/charging measurements of OLC/MnO_2 nano-urchins at ambient temperature is shown in Fig. 3b. In the first discharging curve, there were two plateaus located at 0.75 and 0.48 V, typically ascribed to the complete reduction of Mn^{4+} to Mn^0 as given in Eq. (3) [21,38]. The plateau at 0.75 V disappeared and the one at 0.48 V was shortened in the following discharging cycles, confirming the formation of metallic Mn and Li_2O matrix [21,37]. On the other hand, in the first charging curve the electrode showed a plateau in the potential range between 1.0 and 1.5 V, which was ascribed to the oxidation of Mn^0 to Mn^{2+} [37].These discharging/charging behaviors were consistent with the CV curves shown in Fig. 3a and were superior as compared to that of the pure MnO_2 and pure OLC (Fig. S5c–S5d) [26].

We also calculated the specific capacity to be 1278 and 854 mAh g^{-1} in the first discharging and charging cycles, respectively. It was noted that MnO_2 has a theoretical capacity of 1230 mAh g^{-1} [35]. The slightly larger value in our calculation could be due to the decomposition of electrolyte at a low voltage during the formation of SEI layer, which contributed extra lithium storage at the Mn/Li_2O interface [22]. Similar phenomena have also been reported for other transition metal oxide electrodes [39,40].

A more prominent feature of the OLC/MnO_2 nano-urchins is that the rate capability of LIBs incorporating this material was significantly improved as compared to that of pure MnO_2, as shown in Fig. 3c. The OLC/MnO_2 nano-urchins exhibited a capacity of 1278 mA h g^{-1} in the first discharging cycle, which then gradually reduced to 628 mAh g^{-1} after 10 cycles at a rate of 50 mA g^{-1}. This irreversible capacity, as mentioned above, was due to the

decomposition reactions of electrolyte and the formation of SEI layer [21]. With the increase of discharging/charging rate, however, the irreversibiliy disappeared and the battery could deliver a reversible capacity of 404, 263, 178 and 102 mAh g^{-1} at rates of 200, 500, 1000, and 2000 mA g^{-1}, respectively. Remarkably, the capacity was observed to restore to ~600 mAh g^{-1} and remained stable when the current density returned to 50 mA g^{-1} after 50 cycles (Fig. 3c). This rate capacity of hybrid OLC/MnO_2 nano-urchins was superior to that of the pure MnO_2 taken separately (*e.g.*, <25 mAh g^{-1} for pure MnO_2 at a rate of 1000 mA g^{-1}). It was also better than the layer-by-layer graphene-MnO_2 nanotube film (~520 mAh g^{-1} after continuous 32 cycles at various current densities) [21], and was comparable to the MnO_2/polyaniline anode (~210 mAh g^{-1} at a current density of 1500 mA g^{-1} after 50 cycles) [41].

Furthermore, Fig. 3d shows the electrochemical impedance spectroscopy (EIS) measurements of all three anode materials. The EIS curves presented in Nyquist plots could be fitted to the equivalent circuit (inset of Fig. 3d), where R_s is the electrolyte resistance, R_f and Q_1 are the SEI layer resistance and the constant phase element (CPE), respectively; R_{ct} and Q_2 are the charge transfer resistance and the related double-layer capacitor, respectively; and Q_3 is a CPE corresponding to the line in the low frequency. The fitting results are summarized in Table S2, which indicated that the charge-transfer resistance of the OLC/MnO_2 nano-urchins (~140 Ω) had been greatly reduced from that of pure MnO_2 (~250 Ω) [42].

3.3 Cycling stability

We also compared the cycling performance of pure OLC, pure MnO_2, and hybrid OLC/MnO_2 nano-urchins, as shown in Fig. 4a. While the first two materials displayed a relatively stable cycling performance, an interesting feature was observed for the OLC/MnO_2 nano-urchins. Specifically, the capacity decayed during the first 20 cycles, flattened for the next few cycles,

and then increased to 541 mAh g^{-1} at the 100th cycle. A similar trend was also observed for other metal oxide electrodes but with a much smaller increment than the current observation [39,43]. Although the exact mechanism of such increment still remains unclear, we attributed it to the enhanced conversion reaction of MnO_2 nanoflowers experienced on the electrode. After certain cycles, it is known that the available active sites for lithium ion reaction could increase due to the volume change of the OLC/MnO_2 nano-urchins [17]. This reasonable rise in accessible active sites could thus result in a larger capacity. As a high loading of the MnO_2 nanosheets were anchored uniformly on the surface of OLC, the observed high value of the increment became quite reasonable.

Finally, we plotted the Coulombic efficiency of OLC/MnO_2 nano-urchins at the rate of 200 mA g^{-1}. As shown in Fig. 4b, the Coulombic efficiency increased notably to near 100% after several cycles and remained stable throughout the whole experiments. The high Coulombic efficiency not only indicated a reversible electrolyte decomposition and a complete de-conversion reactions, but also implied the high stability of LIBs [26]. This near-100% Coulombic efficiency also excluded the formation of additional SEI layers during the cycling [17]. In conjunction with the improved stability, our microscopic analysis confirmed that the OLC/MnO_2 nano-urchins preserved discernible shape after 100 cycles (inset of Fig. 4b); whereas pure MnO_2 had completely lost its features and became pulverized (Fig. S6).

3.4 Unique features of OLC

It is known that the lithium storage is critically determined by the transport of lithium ions and electrons at the electrode/electrolyte interface, the kinetics of surface incorporation of lithium ions into the electrochmically active materials, and the specific charge storage mechanism [22]. An ideal electrode architecture should possess a good conductivity to effectively transport electrons to the electrochemically active nanomaterials and a porous (but

not tortuous) structure to enhance the lithium ion diffusion [21,25,44]. *Zhang et al.* used an open 3D interpenetrating nickel network to anchor the MnO_2 nanoparticles and obtained ultrafast charge transport and intercalation/de-intercalaction of active species [45]. Similarly, the porous and open structure of OLC in the present case could possibly contribute: (a) a large surface area for incorporating a high loading of the electrochemically active MnO_2 nanosheets (Fig. 1d); (b) a reduced charge transfer resistance for rapid ion and electron transport without sacrificing the energy density (Fig. 2d); (c) a uniform and isotropic structure that enabled the delivery of lithium ions to the active material and better accommodated the volume change during the charge/discharge cycles (Fig. 3c); and (d) an electrochemically stable core structure (Fig. 4b). The preparation method is also simple and scale as compared to other methods such as sputtering, high-temperature carbonization, or layer-by-layer assembly, as the hybrid OLC/MnO_2 preserved its nanostructural feature after device fabrication. We therefore believe that the 3D isotropic nano-urchins could be highly promising for high-performance rechargeable LIBs.

4. CONCLUSION

In conclusion, we have assembled the OLC/MnO_2 nano-urchins which acted as the stable anode material in LIBs. The electrode showed key electrochemical properties including the improved specific capacity (*i.e.*, from ~260 mAh g^{-1} of the pure MnO_2 to ~630 mAh g^{-1} at the current density of 50 mA g^{-1}), the increased rate capability at various current densities, the stable cycling performance without significant degradation of the nanostructures, and nearly 100% Coulombic efficiency. These improved performance for rechargeable LIBs arose from the unique nanostructure which facilitated fast ion and electron transport and stabilized the MnO_2 nanoparticles during charge storage. Our proven strategy of using OLC as the core

material is cost-effective and generic, which may be applied to other high-capacity transition metal oxides also lead to the *greener and more sustainable development* of energy storage *devices* for advanced applications.

Acknowledgements

This work is supported by the SUTD-ZJU research grant ZJURP1100104, CSIRO's OCE Science Leader Program, and Sensors and Sensor Network Transformational Capability Platform (TCP). ZJH and KO acknowledge the DECRA and Future Fellowships from the Australian Research Council (ARC).

REFERENCES

[1] Tarascon J-M, Armand M. Issues and challenges facing rechargeable lithium batteries. Nature 2001;414:359-67.

[2] Liu C, Li F, Ma L-P, Cheng H-M. Advanced materials for energy storage. Adv Mater 2010;22:E28-62.

[3] Ji L, Lin Z, Alcoutlabi M, Zhang X. Recent developments in nanostructured anode materials for rechargeable lithium-ion batteries. Energy Environ Sci 2011;4:2682-99.

[4] Shapira R, Nessim GD, Zimrin T, Aurbach D. Towards promising electrochemical technology for load leveling applications: extending cycle life of lead acid batteries by the use of carbon nano-tubes (CNTs). Energy Environ Sci 2013;6:587-94.

[5] Wang Z, Wang Z, Liu W, Xiao W, Lou XWD. Amorphous $CoSnO_3$@C nanoboxes with superior lithium storage capability. Energy Environ Sci 2013;6:87-91.

[6] Bruce PG. Energy storage beyond the horizon: Rechargeable lithium batteries. Solid State Ionics 2008;179:752-60.

[7] Liu C-J, Burghaus U, Besenbacher F, Wang ZL. Preparation and characterization of nanomaterials for sustainable energy production. ACS Nano 2010;4:5517-26.

[8] Ostrikov K, Neyts EC, Meyyappan M. Plasma nanoscience: from nano-solids in plasmas to nano-plasmas in solids. Adv Phys 2013;62:113-224.

[9] Han ZJ, Tay BK, Tan CM, Shakerzadeh M, Ostrikov K. Electrowetting Control of Cassie-to-Wenzel Transitions in Superhydrophobic Carbon Nanotube-Based Nanocomposites. ACS Nano 2009;3:3031-6.

[10] Endo M, Kim YA, Hayashi T, Nishimura K, Matusita T, Miyashita K, et al. Vapor-grown carbon fibers (VGCFs) basic properties and their battery applications. Carbon 2001;39:1287-97.

[11] Hu L, Wu H, La Mantia F, Yang Y, Cui Y. Thin, Flexible Secondary Li-Ion Paper Batteries. ACS Nano 2010;4:5843-8.

[12] Ji H, Zhang L, Pettes MT, Li H, Chen S, Shi L, et al. Ultrathin graphite foam: A three-dimensional conductive network for battery electrodes. Nano Lett 2012;12:2446-51.

[13] Wang H, Cui L-F, Yang Y, Casalongue HS, Robinson JT, Liang Y, et al. Mn_3O_4-graphene hybrid as a high-capacity anode material for lithium ion batteries. J Am Chem Soc 2010;132:13978-80.

[14] Kim IT, Magasinski A, Jacob K, Yushin G, Tannenbaum R. Synthesis and electrochemical performance of reduced graphene oxide/maghemite composite anode for lithium ion batteries. Carbon 2013;52:56-64.

[15] Li Y, Zhu C, Lu T, Guo Z, Zhang D, Ma J, et al. Simple fabrication of a Fe_2O_3/carbon composite for use in a high-performance lithium ion battery. Carbon 2013;52:565-73.

[16] Seo DH, Han ZJ, Kumar S, Ostrikov K. Structure-controlled, vertical graphene-based, binder-free electrodes from plasma-reformed butter enhance supercapacitor performance. Adv Energy Mater 2013; DOI: 10.1002/aenm.201300431.

[17] Guo J, Liu Q, Wang C, Zachariah MR. Interdispersed Amorphous MnOx–Carbon Nanocomposites with Superior Electrochemical Performance as Lithium-Storage Material. Adv Funct Mater 2012;22:803-11.

[18] Lavoie N, Malenfant PRL, Courtel FM, Abu-Lebdeh Y, Davidson IJ. High gravimetric capacity and long cycle life in Mn3O4/graphene platelet/LiCMC composite lithium-ion battery anodes. J Power Sources 2012;213:249-54.

[19] Poizot P, Laruelle S, Grugeon S, Dupont L, Tarascon J-M. Nano-sized transition-metal oxides as negative-electrode materials for lithium-ion batteries. Nature 2000;407:496-9.

[20] Truong TT, Liu Y, Ren Y, Trahey L, Sun Y. Morphological and crystalline evolution of nanostructured MnO_2 and its application in lithium-air batteries. ACS Nano 2012;6:8067-77.

[21] Yu A, Park HW, Davies A, Higgins DC, Chen Z, Xiao X. Free-standing layer-by-layer hybrid thin film of graphene-MnO_2 nanotube as anode for lithium ion batteries. J Phys Chem Lett 2011;2:1855-60.

[22] Jamnik J, Maier J. Nanocrystallinity effects in lithium battery materials - Aspects of nano-ionics. Part IV. Phys Chem Chem Phys 2003;5:5215-20.

[23] Guo CX, Wang M, Chen T, Lou XW, Li CM. A Hierarchically Nanostructured Composite of MnO_2/Conjugated Polymer/Graphene for High-Performance Lithium Ion Batteries. Adv Energy Mater 2011;1:736-41.

[24] Reddy ALM, Shaijumon MM, Gowda SR, Ajayan PM. Coaxial MnO_2/carbon nanotube array electrodes for high-performance lithium batteries. Nano Lett 2009;9:1002-6.

[25] Arico AS, Bruce P, Scrosati B, Tarascon J-M, Van Schalkwijk W. Nanostructured materials for advanced energy conversion and storage devices. Nat Mater 2005;4:366-77.

[26] Cabana J, Monconduit L, Larcher D, Palacín MR. Beyond Intercalation-Based Li-Ion Batteries: The State of the Art and Challenges of Electrode Materials Reacting Through Conversion Reactions. Adv Mater 2010;22:E170-92.

[27] Yoshio M, Wang H, Fukuda K. Spherical carbon-coated natural graphite as a lithium-ion battery-anode material. Angew Chem Int Ed 2003;42:4203-6.

[28] Pech D, Brunet M, Durou H, Huang P, Mochalin V, Gogotsi Y, et al. Ultrahigh-power micrometre-sized supercapacitors based on onion-like carbon. Nat Nanotech 2010;5:651.

[29] Wang Y, Yu SF, Sun CY, Zhu TJ, Yang HY. MnO_2/onion-like carbon nanocomposites for pseudocapacitors. J Mater Chem 2012;22:17584-8.

[30] Lou F, Zhou H, Huang F, Vullum-Bruer F, Tran TD, Chen D. Facile synthesis of manganese oxide/aligned carbon nanotubes over aluminium foil as 3D binder free cathodes for lithium ion batteries. J Mater Chem A 2013;1:3757-67.

[31] Subramanian V, Zhu H, Vajtai R, Ajayan PM, Wei B. Hydrothermal synthesis and pseudocapacitance properties of MnO_2 nanostructures. J Phys Chem B 2005;109:20207-14.

[32] Xiao W, Wang D, Lou XW. Shape-controlled synthesis of MnO_2 nanostructures with enhanced electrocatalytic activity for oxygen reduction. J Phys Chem C 2010;114:1694-700.

[33] Lei Z, Zhang J, Zhao XS. Ultrathin MnO_2 nanofibers grown on graphitic carbon spheres as high-performance asymmetric supercapacitor electrodes. J Mater Chem 2012;22:153-60.

[34] Liu Z, Ma R, Ebina Y, Takada K, Sasaki T. Synthesis and delamination of layered manganese oxide nanobelts. Chem Mater 2007;19:6504-12.

[35] Xia H, Lai M, Lu L. Nanoflaky MnO_2/carbon nanotube nanocomposites as anode materials for lithium-ion batteries. J Mater Chem 2010;20:6896-902.

[36] Landi BJ, Ganter MJ, Cress CD, DiLeo RA, Raffaelle RP. Carbon nanotubes for lithium ion batteries. Energy Environ Sci 2009;2:638-54.

[37] Sun B, Chen Z, Kim H-S, Ahn H, Wang G. MnO/C core–shell nanorods as high capacity anode materials for lithium-ion batteries. J Power Sources 2011;196:3346-9.

[38] Xiao X, Lu P, Ahn D. Ultrathin multifunctional oxide coatings for lithium ion batteries. Adv Mater 2011;23:3911-5.

[39] Zhou G, Wang D-W, Li F, Zhang L, Li N, Wu Z-S, et al. Graphene-wrapped Fe_3O_4 anode material with improved reversible capacity and cyclic stability for lithium ion batteries. Chem Mater 2010;22:5306-13.

[40] Wang Y, Yan F, Liu SW, Tan AYS, Song H, Sun XW, et al. Onion-like carbon matrix supported Co_3O_4 nanocomposites: a highly reversible anode material for lithium ion batteries with excellent cycling stability. J Mater Chem A 2013;1:5212-6.

[41] Wang Y-G, Wu W, Cheng L, He P, Wang C-X, Xia Y-Y. A polyaniline-intercalated layered manganese oxide nanocomposite prepared by an inorganic/organic interface reaction and its high electrochemical performance for Li storage. Adv Mater 2008;20:2166-70.

[42] Zhou X, Yin Y-X, Wan L-J, Guo Y-G. Self-assembled nanocomposite of silicon nanoparticles encapsulated in graphene through electrostatic attraction for lithium-ion batteries. Adv Energy Mater 2012;2:1086-90.

[43] Li X, Li D, Qiao L, Wang X, Sun X, Wang P, et al. Interconnected porous MnO nanoflakes for high-performance lithium ion battery anodes. J Mater Chem 2012;22:9189-94.

[44] Tarascon J-M. Key challenges in future Li-battery research. Phil Trans R Soc A 2010;368:3227-41.

[45] Zhang H, Yu X, Braun PV. Three-dimensional bicontinuous ultrafast-charge and -discharge bulk battery electrodes. Nat Nanotech 2011;6:277-81.

Figure captions:

Fig. 1 - (a) Schematic diagram of the synthesis procedure of the core-leaf OLC/MnO_2 hybrid nano-urchins. Scanning electron micrographs of (b) pure OLC, (c) intermediate product, and (d) final hybrid nano-urchins. Inset in (d) is the magnified image of a single urchin-like nano-architecture.

Fig. 2 - (a) Low- and (b) high-resolution TEM images of pure OLC, and (c) – (e) OLC/MnO_2 nano-urchins. Inset in (c) illustrates the intricate, 3D core-leaf architecture. (f) Electron diffraction pattern and (g) EDX spectrum of the OLC/MnO_2 structures.

Fig. 3 - (a) Cyclic voltammetry curves of the OLC/MnO_2 nano-urchin electrode in the first three cycles at a scan rate of 0.05 mV s^{-1} in a potential range of 0.01 – 3 V *vs* Li/Li^+. (b) Galvanostatic discharging/charging curves of the OLC/MnO_2 nano-urchin electrode at a current density of 50 mA g^{-1} for the first 10 cycles. Inset in (b) is the photo of CR2032 button battery assembled in this work. (c) Rate capabilities of the pure MnO_2, pure OLC, and OLC/MnO_2 nano-urchin electrodes. (d) EIS spectra and fittings of the pure MnO_2, pure OLC and OLC/MnO_2 nano-urchin electrodes. Inset in (d) shows the equivalent circuit model used for the fittings.

Fig. 4 - (a) Cyclic performance of the pure MnO_2, pure OLC and OLC/MnO_2 nano-urchin electrodes at 200 mA g^{-1}. (b) Coulombic efficiency of the OLC/MnO_2 nano-urchin electrode at 200 mA g^{-1}. Inset in (b) is the SEM image of OLC/MnO_2 nano-urchin electrode after 100 cycles.

Figures:

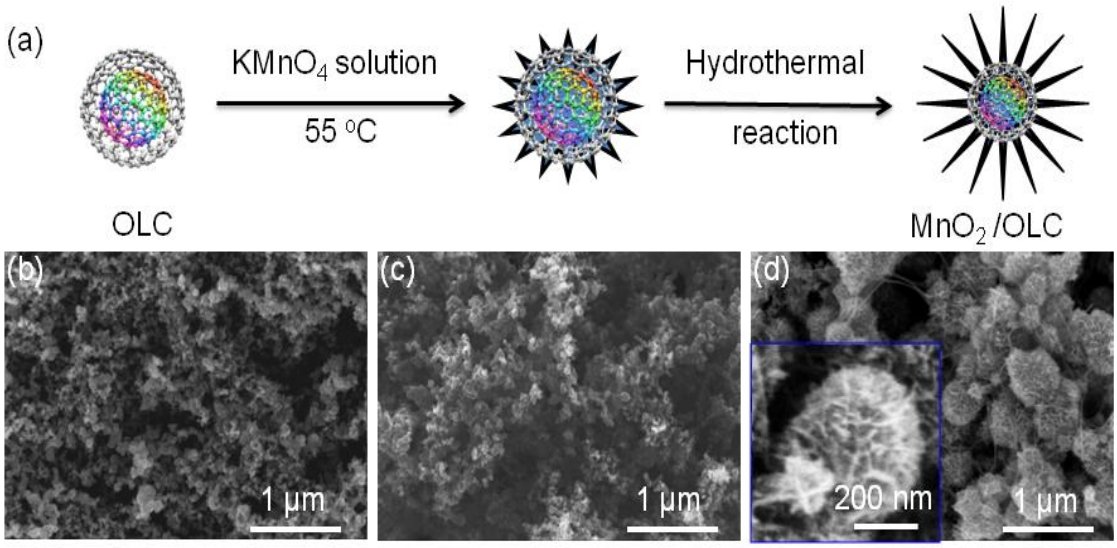

Fig. 1 - (a) Schematic diagram of the synthesis procedure of the core-leaf OLC/MnO_2 hybrid nano-urchins. Scanning electron micrographs of (b) pure OLC, (c) intermediate product, and (d) final hybrid nano-urchins. Inset in (d) is the magnified image of a single urchin-like nano-architecture.

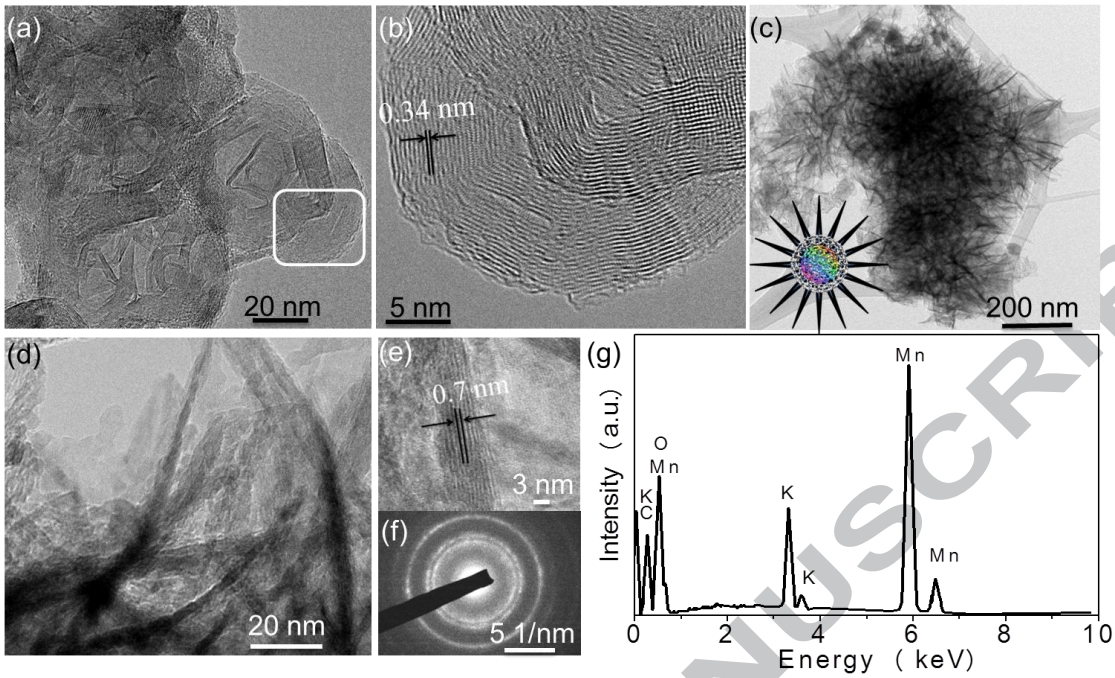

Fig. 2 - (a) Low- and (b) high-resolution TEM images of pure OLC, and (c) – (e) OLC/MnO_2 nano-urchins. Inset in (c) illustrates the intricate, 3D core-leaf architecture. (f) Electron diffraction pattern and (g) EDX spectrum of the OLC/MnO_2 structures.

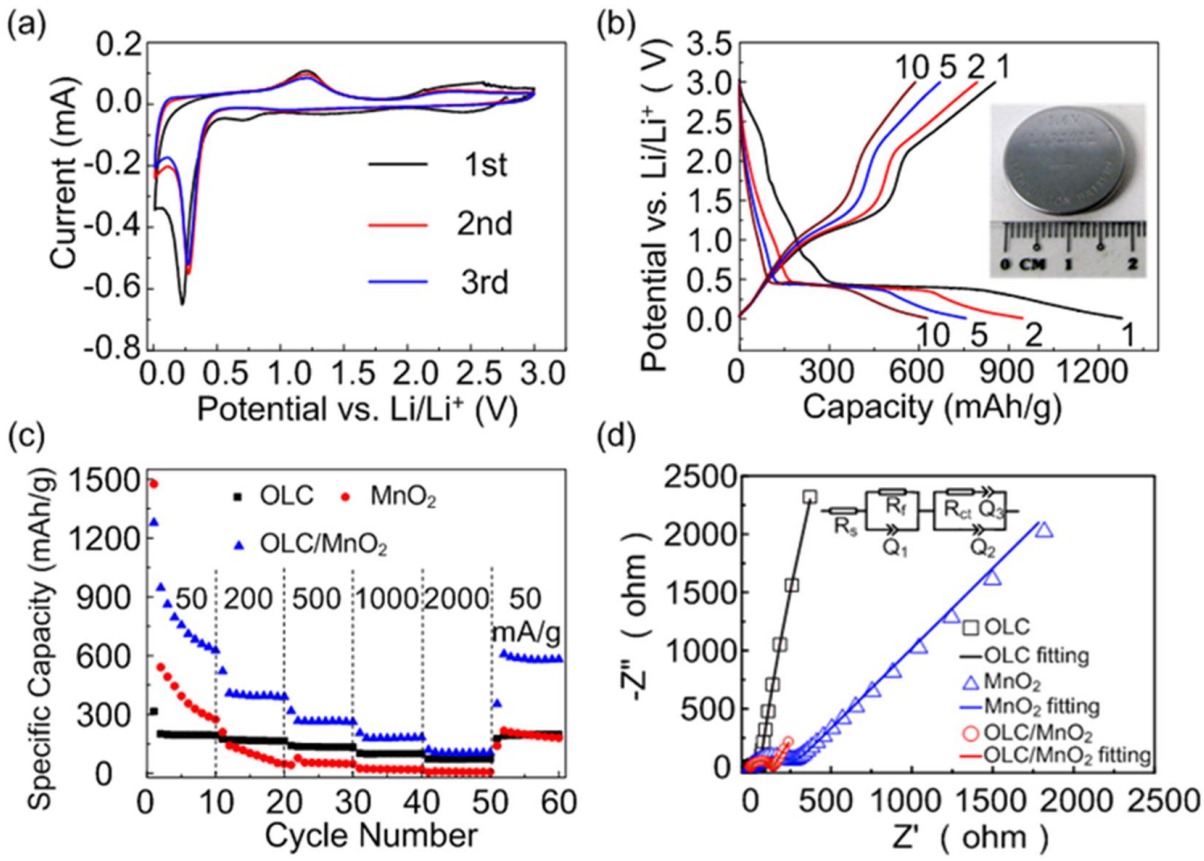

Fig. 3 - (a) Cyclic voltammetry curves of the OLC/MnO_2 nano-urchin electrode in the first three cycles at a scan rate of 0.05 mV s^{-1} in a potential range of 0.01 – 3 V *vs* Li/Li^+. (b) Galvanostatic discharging/charging curves of the OLC/MnO_2 nano-urchin electrode at a current density of 50 mA g^{-1} for the first 10 cycles. Inset in (b) is the photo of CR2032 button battery assembled in this work. (c) Rate capabilities of the pure MnO_2, pure OLC, and OLC/MnO_2 nano-urchin electrodes. (d) EIS spectra and fittings of the pure MnO_2, pure OLC and OLC/MnO_2 nano-urchin electrodes. Inset in (d) shows the equivalent circuit model used for the fittings.

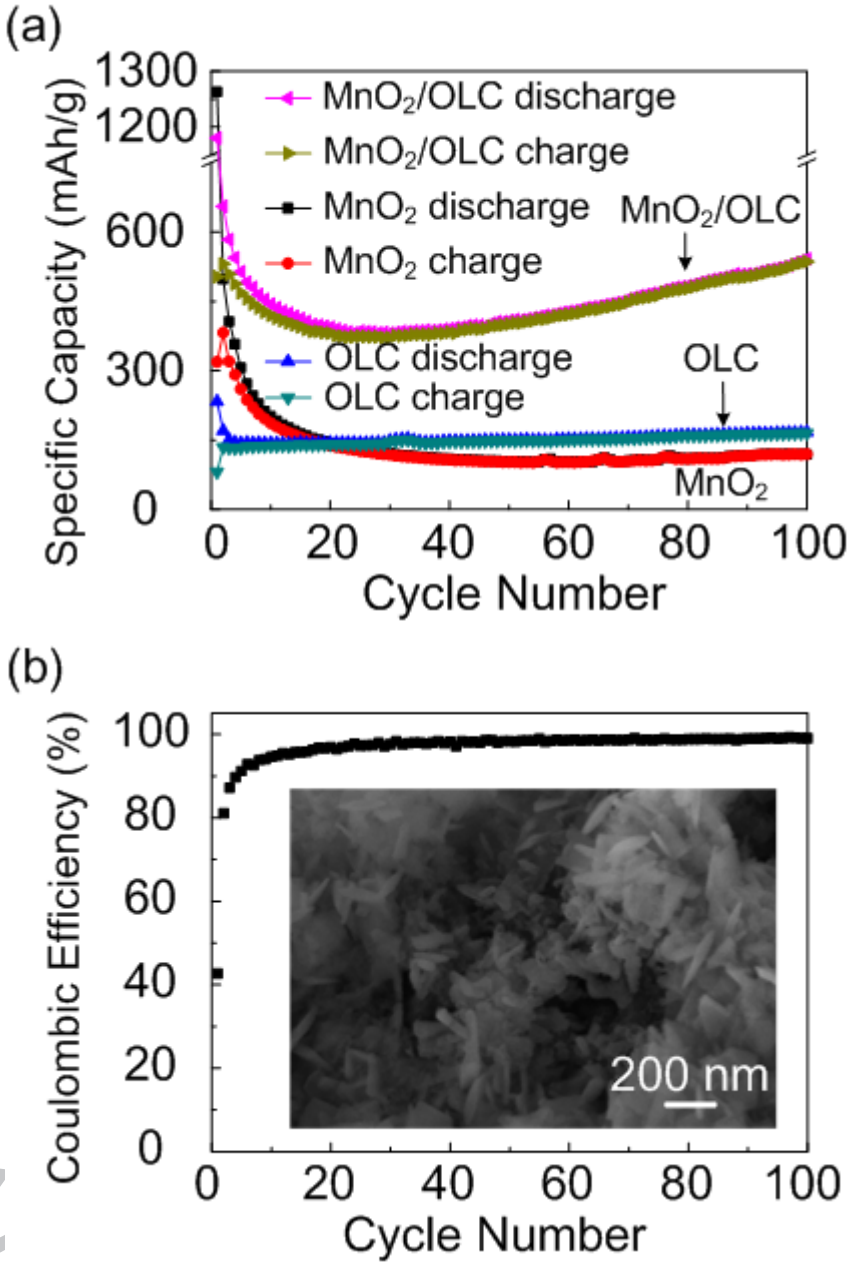

Fig. 4 - (a) Cyclic performance of the pure MnO_2, pure OLC and OLC/MnO_2 nano-urchin electrodes at 200 mA g^{-1}. (b) Coulombic efficiency of the OLC/MnO_2 nano-urchin electrode at 200 mA g^{-1}. Inset in (b) is the SEM image of OLC/MnO_2 nano-urchin electrode after 100 cycles.